DIRECTIONAL SOURCE SIMULATION IN FDTD ROOM ACOUSTIC MODELING VIA WEIGHTED FIRST-ORDER REFLECTIONS

Stephen Oxnard

Meridian Audio Ltd.
Huntingdon, UK
stephen.oxnard@meridian.co.uk

ABSTRACT

This paper proposes a means of simulating directional sources in Finite Difference Time Domain (FDTD) based acoustic models for impulse response (IR) calculation which, unlike other currently available methods, is able to accommodate highly irregular directivity patterns. Weighted numerical free-field IRs are applied to the simulation of first-order reflections at the boundaries of a modeled acoustic domain such that the continuing interior wave field is that which would be produced by a directional sound source. Numerical results demonstrate the application of this approach for a 2-Dimensional wave field, implementing both simple and irregular (e.g. highly directional, discontinuous) sound source directivity patterns.

1. INTRODUCTION

Directional sound source modeling is of importance for realistic wave-based room acoustics simulations. Previous work in this area has largely focused on emulating source directivity functions via weighted monopole excitations [1, 2, 3] and spherical harmonic composition [4, 5]. These strategies are capable of simulating analytical directivity functions but are not well-suited to emulating realistic source directivities that include large fluctuations in magnitude over small angles. Some of them (e.g. [3, 4]) provide only first-order spherical harmonic directivity patterns. A method for frequency-dependent directional source modeling based on empirical directivity functions is presented in [6] by which it is shown possible to model smooth variances in source directivity in the far-field. Recent work [7, 8] provides a means of FDTD-based directional sound source modeling that is capable of incorporating source movement and rotation for multipole source directivities. An alternative approach is presented in [9] and is based on the optimization of initial values within the target acoustic field represented by a FDTD scheme. While the strategies of [6, 7, 8, 9] have been shown as capable of representing source directivity patterns that vary slowly with angle (i.e. well-behaved and continuous), it has yet to be demonstrated that such approaches are suitable for representing more challenging patterns such as those which vary rapidly with small changes in angle.

This paper presents a directional source modeling strategy for FDTD acoustics simulations which attains the primary goal of representing highly directional/complex source directivity patterns for static source IR capture. To the author's knowledge, this outcome is unattainable using existing techniques. It is intended that this strategy be extended to 3D and exploited for numerical room impulse response prediction with representation of realistic sound sources.

Copyright: © 2019 Stephen Oxnard et al. This is an open-access article distributed under the terms of the Creative Commons Attribution 3.0 Unported License, which permits unrestricted use, distribution, and reproduction in any medium, provided the original author and source are credited.

In brief, this approach begins by pre-calculating the free-field response to a monopole excitation at all boundary locations defined in the target acoustic field. As such, the outgoing direct sound component from a given monopole sound source location is captured in its entirety for each discrete boundary node and its neighbouring nodes in a given FDTD scheme. During simulation of the target acoustic field, pre-calculated responses are weighted and summed into the field at corresponding boundary nodes during run time to cancel a proportion of the outgoing direct sound component produced by a monopole sound source. In doing so, the amplitude of the subsequent first-order reflection may be weighted around the azimuth with respect to the sound source location and directivity pattern. The result is a first-order reflection and subsequent wave field that would be produced in response to a directional impulsive sound source. The following contribution details the formulation of this approach and continues to verify its correctness via a series of test cases.

2. SCHEME FORMULATION

2.1. The FDTD Model

For the purposes of simple and rapid exposition of this directional source model, this derivation is limited to the so-called "leap-frog" explicit FDTD iterative wave equation solution (see e.g. [10]) for a 2D target acoustic field. This solution solves the 2nd-order wave equation, $\frac{\partial^2 p}{\partial t^2} = c^2 \nabla^2 p$, for a scalar acoustic pressure field, p, and sound propagation speed, c, using the iterative update equation:

$$p_{l,m}^{n+1} = \lambda^2 S_{l,m}^n + (2 - 4\lambda^2) p_{l,m}^n - p_{l,m}^{n-1} \tag{1}$$

where $\lambda = \frac{cT}{h}$ for discrete time step, $T = 1/F_s$, spatial sampling instance h and temporal sampling rate Fs. The location of a pressure sample, or 'node', $p_{l,m}^n$, in time and space is given by the integer indexes n, for time nT, and (l, m) for the Cartesian x- and y-coords (lh, mh) in 2D space. Finally, the term $S_{l,m}^n$ refers to the sum of pressure values neighbouring a given node at current time n on a rectilinear grid of nodes defined over an enclosed domain:

$$S_{l,m}^n = p_{l+1,m}^n + p_{l-1,m}^n + p_{l,m+1}^n + p_{l,m-1}^n \tag{2}$$

Following [11], locally reacting surface (LRS) boundary conditions (after [12]) may be applied in such a model at terminating edges and corners of the spatial domain. This facilitates the modeling of absorbing surface characteristics within the acoustic simulation. The so-called "velocity-centered" [13] formulation of the

LRS condition may be written as follows for a right-hand boundary with frequency independent surface impedance ζ:

$$p_{l,m}^{n+1} = \alpha_E \Big(\lambda^2 (p_{l-1,m}^n + p_{l,m+1}^n + p_{l,m-1}^n) + (2-3\lambda^2) p_{l,m}^n - \beta_E p_{l,m}^{n-1} \Big) \quad (3)$$
$$\alpha_E = \frac{1}{1+\frac{\lambda}{2\zeta}}, \quad \beta_E = 1 - \frac{\lambda}{2\zeta}$$

For a top-right-hand corner boundary node, the LRS condition is given as:

$$p_{l,m}^{n+1} = \alpha_C \Big(\lambda^2 (p_{l-1,m}^n + p_{l,m-1}^n) + (2-3\lambda^2) p_{l,m}^n - \beta_C p_{l,m}^{n-1} \Big); \quad \alpha_C = \frac{1}{1+\frac{\lambda}{\zeta}}, \quad \beta_C = 1 - \frac{\lambda}{\zeta} \quad (4)$$

Similar expressions may be derived for all other boundary orientations aligned with the rectilinear grid as per [14]. The LRS boundary conditions together with (1) complete the FDTD model used for this study.

2.2. Derivation of Directional Sound Source Solution

The premise of this work is that it is possible to manipulate the first-order reflection exiting a boundary node in response to an omnidirectional impulsive excitation using pre-computed free-field responses such that the reflected wave front, and subsequent wave field, represents that produced by a directional sound source. The required free-field responses are those which preserve continuity of the wave equation at the location of each boundary node for all values of impedance in the range $\zeta = [1, \infty]$. These responses are denoted $E_{l,m}^n$ for edges and $C_{l,m}^n$ for corners. The treatment of right-hand boundaries is the focus of the following derivation, noting that similar free-field response expressions may be reached by the same means for all remaining boundary orientations.

The derivation of $E_{l,m}^n$ is presented here for the case of a right-hand edge boundary with the governing equation (3). Comparing (3) to the discrete wave equation update (1) it is evident the function of responses required to preserve wave motion at the edge boundary, denoted P_E, is:

$$P_E = \Big(1-\alpha_E\Big)\Big(\lambda^2 (p_{l-1,m}^n + p_{l,m+1}^n + p_{l,m-1}^n) + (2-3\lambda^2) p_{l,m}^n - 2p_{l,m}^{n-1}\Big) + \lambda^2 (p_{l+1,m}^n - p_{l,m}^n) \quad (5)$$

and that by adding P_E to the right hand side of (3), the wave equation results and anechoic conditions are realized at the boundary. However, such a result cannot be computed using responses of the enclosed pressure field p during simulation as these responses would comprise both direct and reflected wave fronts as opposed to the free-field direct sound components as required. Furthermore, the term $p_{l+1,m}^n$ refers to a response that lies outside the simulated domain and is undefined in the numerical solution of the pressure field p as prescribed by equations (1)-(4). Hence, it is proposed that all pressure signals contributing to P_E be computed in the free-field in advance of simulating the problem domain p. Denoting the free-field as $\tilde{p}$, the free-field equivalent of P_E is then the desired signal $E_{l,m}^n$:

$$E_{l,m}^n = \Big(1-\alpha_E\Big)\Big(\lambda^2 (\tilde{p}_{l-1,m}^n + \tilde{p}_{l,m+1}^n + \tilde{p}_{l,m-1}^n) + (2-3\lambda^2) \tilde{p}_{l,m}^n - 2\tilde{p}_{l,m}^{n-1}\Big) + \lambda^2 (\tilde{p}_{l+1,m}^n - \tilde{p}_{l,m}^n) \quad (6)$$

for a right-hand edge boundary node at location (lh, mh) and time nT.

A similar procedure is followed for the case of a corner boundary node. In this instance, using a top-right-hand boundary node (4), the function required to preserve continuity of the wave equation at the boundary node, P_C, is:

$$P_C = \Big(1-\alpha_C\Big)\Big(\lambda^2 (p_{l-1,m}^n + p_{l,m-1}^n) + (2-2\lambda^2) p_{l,m}^n - 2p_{l,m}^{n-1}\Big) + \lambda^2 (p_{l+1,m}^n + p_{l,m+1}^n - 2p_{l,m}^n) \quad (7)$$

Again, the required free-field equivalent pressure signals comprising P_C are pre-computed to produce the desired signal $C_{l,m}^n$:

$$C_{l,m}^n = \Big(1-\alpha_C\Big)\Big(\lambda^2 (\tilde{p}_{l-1,m}^n + \tilde{p}_{l,m-1}^n) + (2-2\lambda^2) \tilde{p}_{l,m}^n - 2\tilde{p}_{l,m}^{n-1}\Big) + \lambda^2 (\tilde{p}_{l+1,m}^n + \tilde{p}_{l,m+1}^n - 2\tilde{p}_{l,m}^n) \quad (8)$$

Having pre-computed the required signals $E_{l,m}^n$ and $C_{l,m}^n$ in the free-field for all edge and corner boundary nodes that facilitate a first-order reflection in the target acoustic field, they may be weighted based on an arbitrary source directivity function, $S(\theta)$, for $\theta \in [0, 2\pi]$ and $S(\theta) \in [-1, 1]$. In order to achieve variable cancellation of the initial sound wave incident on the boundary, appropriate weighting coefficients for $E_{l,m}^n$ and $C_{l,m}^n$ are defined as $A(\theta) = 1 - S(\theta)$. Hence, the final update expression for a right-hand edge boundary node of the target domain p during simulation is:

$$p_{l,m}^{n+1} = \alpha_E \Big(\lambda^2 (p_{l-1,m}^n + p_{l,m+1}^n + p_{l,m-1}^n) + (2-3\lambda^2) p_{l,m}^n - \beta_E p_{l,m}^{n-1} \Big) + A(\theta) E_{l,m}^n \quad (9)$$
$$\alpha_E = \frac{1}{1+\frac{\lambda}{2\zeta}}, \quad \beta_E = 1 - \frac{\lambda}{2\zeta}$$

where θ is taken to be the angle between the look direction of the sound source and the location of the respective boundary node w.r.t the source location. For a top-right-hand corner boundary node, the following update expression is applied during simulation:

$$p_{l,m}^{n+1} = \alpha_C \Big(\lambda^2 (p_{l-1,m}^n + p_{l,m-1}^n) + (2-3\lambda^2) p_{l,m}^n - \beta_C p_{l,m}^{n-1} \Big) + A(\theta) C_{l,m}^n \quad (10)$$
$$\alpha_C = \frac{1}{1+\frac{\lambda}{\zeta}}, \quad \beta_C = 1 - \frac{\lambda}{\zeta}$$

The same approach is applied to edge and corner boundary nodes of all other possible orientations.

Examples of the application of the weighted free-field responses include full reflection and anechoic conditions. Full reflection results when $S(\theta) = 1$ and $A(\theta) = 0$ such that the functions $E_{l,m}^n$ and $C_{l,m}^n$ do not contribute to the response at the associated boundary node and, therefore, do not cancel or reduce the reflection. Conversely, for $S(\theta) = 0$ and $A(\theta) = 1$, full cancellation is required and hence the maximum contribution of the functions $E_{l,m}^n$ and $C_{l,m}^n$ are applied to associated boundary nodes thus nullifying the first-order reflection from these nodes yielding anechoic conditions in the subsequent simulated wave field.

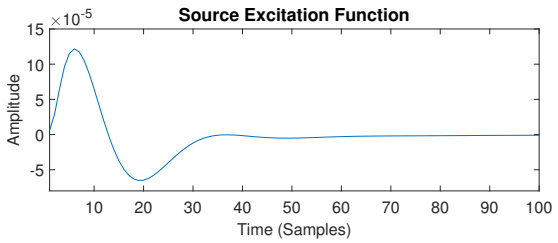

Figure 1: The DC-blocked and low pass filtered Kronecker Delta input excitation function with afterglow removal applied, after [15]. This source function is implemented as a soft-source in all simulations of the target acoustic domain documented in this paper.

2.3. Directional Sound Source IR Simulation

Using the solution described, the initial wavefront incident on each boundary node may be fully or partially cancelled such that a directional source response is imposed on the target acoustic field for all time after the first-order reflections. It is important to note that this approach is valid, in the form described here, for concave domain geometries (see section 5 for more discussion).

Implementing the directional sound source requires functions $E^n_{l,m}$ and $C^n_{l,m}$ to be pre-computed for every boundary node that facilitates a first-order reflection as a consequence of the initial excitation. This pre-computation is conducted using a large leap-frog FDTD scheme that allows capture of node responses for the passage of the direct sound component only. Note that such free-field responses need be only recorded until they reach a negligible amplitude (e.g. -60 dB relative to the peak amplitude value). This condition affects the size of the free-field scheme as it must be large enough to render the free-field IR at all boundary node locations in absence of any unwanted reflections which may arise from domain terminations. Next, the recorded functions $E^n_{l,m}$ and $C^n_{l,m}$ are weighted by $A(\theta)$, with reference to the source location, and applied during simulation as per equations (9) and (10). Note that the free-field responses preserve time alignment with the simulated pressure field p. The resulting IR/s may then be captured as required from any point within the modeled space. These IRs contain the characteristics of the source directivity function $S(\theta)$ for all time after the onset of the first reflection.

A final post-processing step is needed in order to produce an appropriately weighted direct sound component in the resulting IR/s. This is conducted by obtaining the free-field responses at receiver locations during the pre-computation process. These free-field direct sound components may be weighted by $A(\theta)$, where θ is the angle between the receiver locations and the source look direction, and subtracted from the recorded IRs. This completes the directional sound source model for IR capture in FDTD acoustic simulations.

3. EXPERIMENTAL PROCESS

3.1. The FDTD Simulation

The simulated 2D FDTD scheme incorporates an inter-nodal sampling index defined at the Courant limit, yielding the smallest spatial sampling index that preserves numerical stability, $h = \sqrt{2}cT$, for a given $T = \frac{1}{F_s}$ in accordance with von Neumann stability analysis as applied to (1)[16]. For the purposes of this work, a sampling rate of $F_s = 48$ kHz and wave speed $c = 344$ ms^{-1} is applied giving $h = 0.0101$ m. This provides a usable simulation output bandwidth of 0.1 F_s = 4.8 kHz providing a maximum deviation of relative wave phase velocity of ≤ 2 % [17, 18]. The modeled domain is of side length 101 nodes with a central source location given by $(l, m) = (51,51)$ and velocity-centered LRS boundary conditions applied to terminating edges and corners.

The input source excitation is implemented using a soft-source [19] pre-filtered Kronecker delta function. The Kronecker delta function is pre-treated with a DC-blocking filter and a low-pass, 3rd-order Butterworth filter with cut-off frequency f_c = 0.075 F_s to minimize the impact of numerical dispersion effects. Finally, the resulting impulse is treated using afterglow removal to provide a more transient excitation free from afterglow that is intrinsic to the Green's function for the 2D wave equation [15]. Figure 1 depicts the first 100 samples of the resulting input source function. As shown, the filtering applied to the Kronecker delta function produces a function that is smeared in time and maintains a low negative amplitude for time $n \simeq$ [70:100]. These characteristics are important when interpreting results presented in Section 4.

3.2. Implementation of the Directional Sound Source

Having rendered functions $E^n_{l,m}$ and $C^n_{l,m}$ for every corresponding boundary node, they are then weighted appropriately according to $A(\theta) = 1 - S(\theta)$ and summed with the response of the corresponding boundary node during run-time. As the excitation of the FDTD simulation is a pre-filtered Kronecker delta function applied to one central source node, the initial wave propagation will be that of a free-field monopole. The impact of summing $E^n_{l,m}$ and $C^n_{l,m}$ into the corresponding boundary node's response is that the first-order reflection, on exit from the boundary, is weighted as required over the azimuth. A series of five test cases are defined to analyse particular simulation scenarios.

4. VALIDATION OF THE DIRECTIONAL SOUND SOURCE

Due to the fact that this approach to directional sound source simulation relies on weighted first-order reflections within the simulated target acoustic field, it is not possible to take a commonly employed method of analysis such as the measurement of the direct sound around the azimuth using a circular crux of receiver locations (see e.g. [3], [6]). Furthermore, measurement of the reflected wavefront amplitudes around the azimuth immediately after the first-order reflection does not provide a sensible representation of the expected directivity pattern. The reason for this can be explained using Huygen's Principle: an outgoing reflection from a single boundary node will proceed as a half-space monopole and therefore spread and sum with the reflections from adjacent boundary nodes thus producing the reflected wavefront in its totality. As a result, the directivity function will become immediately obscured within the target acoustic domain as directionally weighted first-order reflections spread and sum together. Hence, a series of indirect approaches to validating the proposed directional source method are examined and discussed in the following. All test cases are performed with boundary impedance ζ = 39 giving reflection coefficient R = 0.95 in order to ensure correct operation in conjunction with LRS boundary conditions.

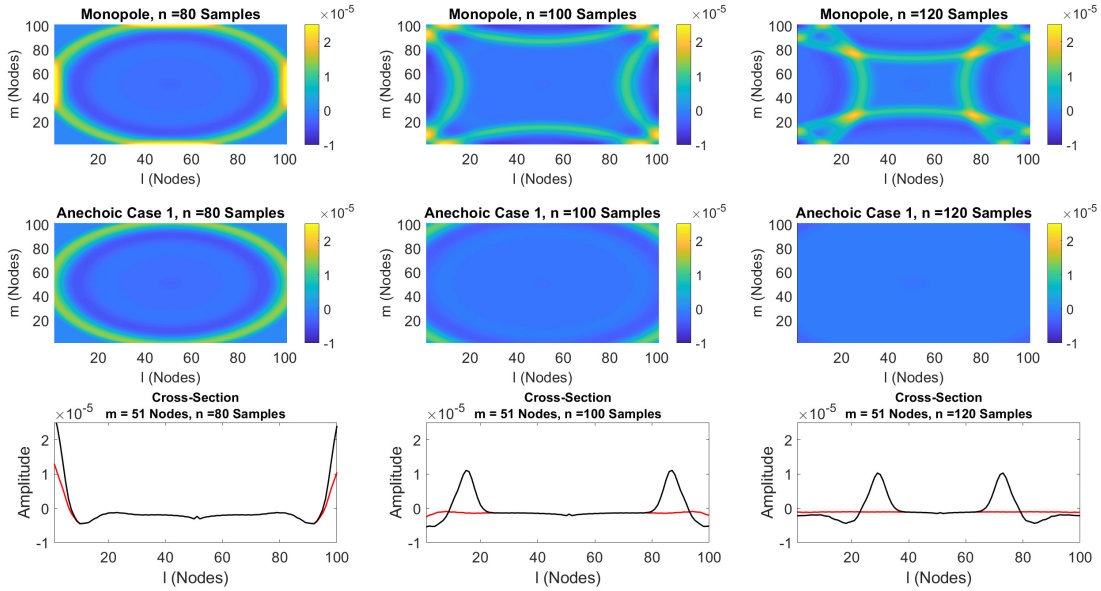

Figure 2: Results of CASE 1. Top row: Monopole sound source excitation with no directional weighting. Middle row: Monopole sound source excitation with full cancellation via free field response functions $E^n_{l,m}$ and $C^n_{l,m}$ applied at all boundary nodes. Bottom row: Cross-sectional amplitude values for the monopole (black) and anechoic (red) simulations. Time sample and node indexes are given in the diagram and all amplitude axes are equal.

CASE 1: Producing Anechoic Boundaries via Full Cancellation of First-Order Reflection

This first test case seeks to verify that the summation of response functions $E^n_{l,m}$ and $C^n_{l,m}$ weighted by $A(\theta) = 1$ for all angles around the azimuth with the simulated target acoustic field p produces anechoic conditions after the passage of the direct sound component. The condition $A(\theta) = 1$ corresponds to a directivity function $S(\theta) = 0$, i.e. the sound source is nullified in all directions due to full cancellation of the first-order reflection at the boundary nodes by $E^n_{l,m}$ and $C^n_{l,m}$. Figure 2 shows the result of implementing this directivity condition in the simulated target acoustic field (middle row) alongside the same target acoustic field excited by the input function only resulting in a monopole response (top row). Time sample instances of 80, 100 and 120 samples are selected to view the progression of the wavefronts throughout the simulated domain. It is clear from the monopole response that strong reflections are present within the domain as time increases. Conversely, in the case where the directivity function is applied, the first-reflection is completely cancelled yielding anechoic conditions as expected. This result is explored further by examining the cross-sectional amplitude values from both simulations across the middle of the domain (l = [1:100], m = 51). It is clear that reflections are preserved in the monopole response simulation (black) and that the same reflections are completely cancelled in the anechoic case (red). The small deviation from zero amplitude observed in the anechoic case cross-section is due to the remaining outgoing samples from the monopole sound source which maintains non-zero amplitude values up to and beyond $n \simeq 100$ samples. This crucial result demonstrates that the proposed directional source strategy may be employed to vary the strength of first-order reflections on a node-by-node basis hence facilitating highly directional source characteristics.

CASE 2: Summing Individual Boundary Node Reflections to Produce a Monopole Response

In order to further demonstrate the ability of the proposed approach to emulate directional sound source characteristics on a node-by-node basis over the boundaries of a modelled domain, the following test case simulates the result of applying $E^n_{l,m}$ to each edge node and $C^n_{l,m}$ to each corner node on an individual basis. As such, each individual response emulates a source directivity function for which $S(\theta) = 1$ ($A(\theta) = 0$) in the direction of a single boundary node and $S(\theta) = 0$ ($A(\theta) = 1$) otherwise. Figure 3 shows two examples of such cases. As shown, the outgoing monopole wavefront progresses to the boundary and is cancelled by all nodes but one located at $[l, m] = [1, 51]$ in one simulation (top row) and $[l, m] = [100, 51]$ in another (middle row). Examining both cases, it is demonstrated that a single half-space monopole reflection spreads from the individual boundary nodes in each simulation. The low amplitude of the reflections is as expected when all other boundary nodes are set to the anechoic condition and thus collectively dissipate a significant amount of energy from the initial source excitation. Referring to the bottom row of Figure 3, the single node reflection from the left boundary is displayed by the cross-section amplitude plots (depicted in black). The reflection passes back into the domain and sums with the continuing wavefront produced by the source. Finally, the amplitude of the reflection from the right boundary (cross-section, depicted in red)

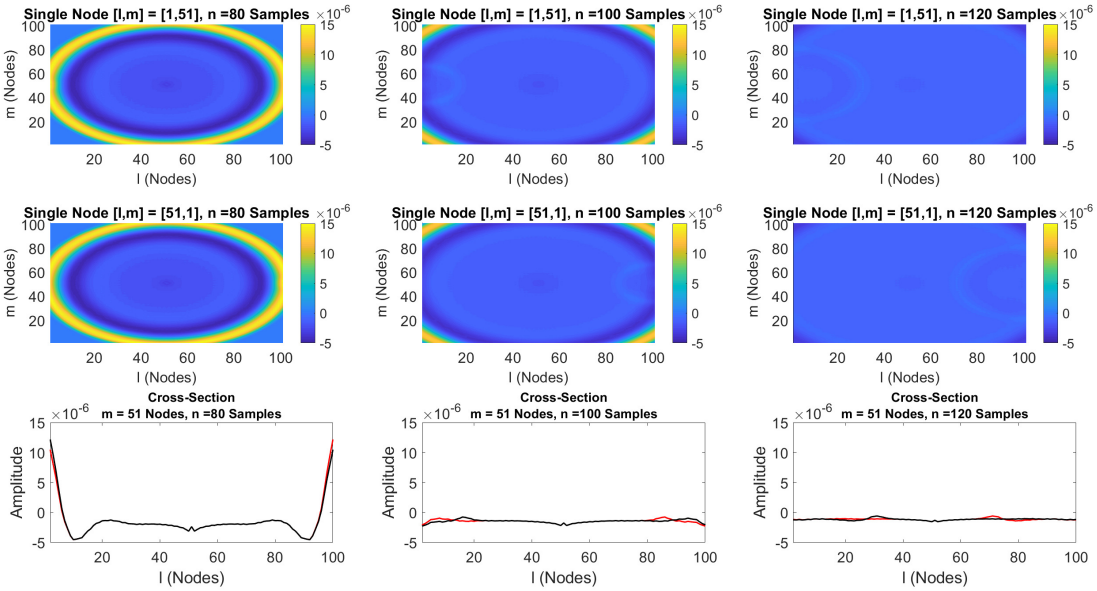

Figure 3: Results of CASE 2. Top row: Individual node reflection at boundary location l, m = [1,51]. Middle row: Individual node reflection at boundary location l, m = [100,51]. In both cases, the free-field response function $E^n_{l,m}$ is applied with $S(\theta) = 1$ ($A(\theta)$ = 0). Bottom row: Cross-sectional amplitude values for the top row (black) and middle row (red) simulations. Time sample values and nodes are given in the diagram and all amplitude axes are equal.

is seen to be symmetrical to that of the left boundary reflection w.r.t. the centre of the modeled domain. To proceed, the wave field produced by each individual node reflection is simulated and the result is recorded for all nodes at time n = 120 samples. Recall that each wave field consists of the superposition of the individual node reflection and the continuing source excitation. As such, when all individual wave fields are summed, the source excitation is summed in once for every boundary node. This can be accounted for by subtracting $N - 1$ copies of the anechoic response (see Figure 2) at time n = 120 samples where N is the number of contributing boundary nodes. Note that this subtraction is only required for the purposes of demonstrating this test case. It may be stated that the sum of N individual contributions equates to a monopole when $N - 1$ anechoic responses are subtracted from the result. This outcome is verified by subtracting the summed responses from the monopole response generated in Case 1 at time sample n = 120 (see Figure 4 below).

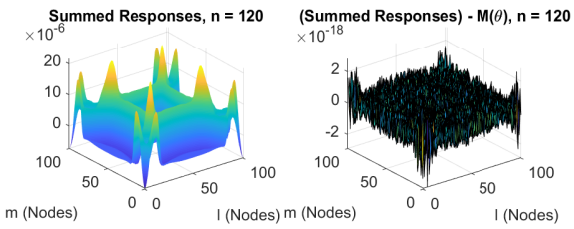

Figure 4: Summed individual boundary node reflections (left) and the difference (right) between the summed responses and the monopole $M(\theta)$. Note, axis scales are not consistent.

As shown in Figure 4, the subtraction of the wave field produced by the treated sum of responses from that of the monopole results in a zero pressure field (the cumulative noise floor of the contributing wave fields). This test case result demonstrates that the superposition of individual node reflections produces a monopole directivity function. Hence, the approach has been shown to be correct and suitable for producing directivity patterns that are highly directional (for example the arc length of one node relative to the sound source location).

CASE 3: Summing Opposing Semi-Circular Directivity Pattern Responses to Produce a Monopole Response

This test case is devised to demonstrate that the directional sound source implementation is capable of reproducing target directivity functions that incorporate discontinuities. In brief, a left-going semi-circular source directivity function is modeled by setting $S(\theta)$ = 1 for all boundary nodes with $0 < l < 51$ and applying $E^n_{l,m}$ and $C^n_{l,m}$ as prescribed in section 2. A further semi-circular source directivity is defined as right-going when $S(\theta)$ = 1 for all boundary nodes with $51 < l \leq 100$. Left- and right-going directivities are denoted $S_L(\theta)$ and $S_R(\theta)$ respectively. The corresponding simulated wave fields are shown in Figure 5 for time sample n = 120. As depicted, the first-order reflected wavefronts for $S_L(\theta)$ and $S_R(\theta)$ are nullified from the right and left boundaries respectively. In addition, it is clear that the reflected wavefronts in the region of l = 51 exhibit diffraction around the discontinuity imposed by the target directivity function. This is to be expected from preserving the continuity of the target pressure field. As a means of verifying the correctness of the simulated wave fields in response to the two tar-

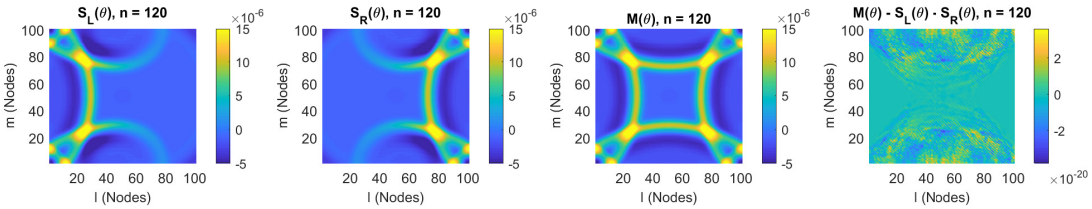

Figure 5: Results of CASE 3. (From left to right) The simulated wave fields produced by weighting boundary first-order reflections by $S_L(\theta)$, $S_R(\theta)$, $M(\theta)$ and $M(\theta) - (S_L(\theta) + S_R(\theta))$ at time sample n = 120. Note, the amplitude axis of the right-most panel is of order 10^{-20}

.

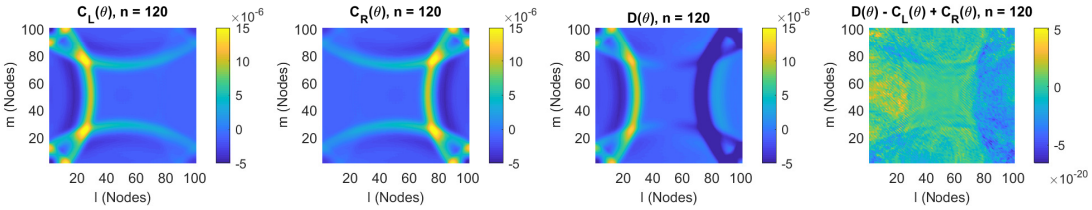

Figure 6: Results of CASE 4. (From left to right) The simulated wave fields produced by weighting boundary first-order reflections by $C_L(\theta)$, $C_R(\theta)$, $D(\theta)$ and the result of combining these responses to generate a zero pressure wave field. Note, the amplitude axis of the right-most panel is of order 10^{-20}

.

get source directivities, their sum is subtracted from a response to a monopole $M(\theta)$. As with CASE 2, it is necessary to account for the continuing sound source present in both semi-circular source simulations. The addition of the two wave fields doubles the contribution of the source. As such, a single anechoic response is subtracted from the sum of the two directional sound source simulations, noting again that this additional process is only necessary for the purposes of verification. The difference between the resulting wave field and the wave field in response to $M(\theta)$ is a zero pressure field (the noise floor of the simulations) as shown in the right most panel of Figure 5. This completes the empirical proof that the directional sound source approach is capable of emulating complex directivity functions.

CASE 4: Summing Opposing Cardioid and Dipole Directivity Responses to Produce a Zero Pressure Field

Up to this point, test case directivities have incorporated only positive values for $S(\theta)$. In this test case, it is demonstrated that the directional sound source implementation is suitable for negative directivity function values. This is achieved by simulating a left-going cardioid response $C_L(\theta) = 0.5 + 0.5\cos(\theta)$, a right-going cardioid response $C_R(\theta) = 0.5 + 0.5\cos(\theta + \pi)$ and a circular bi-directional response $D(\theta) = \cos(\theta)$. Figure 6 displays the resulting wave fields rendered at time sample n = 120. It is straightforward to show that the combination $D_L(\theta) - C_L(\theta) + C_R(\theta)$ = 0. Following on from this, it is assumed that if the rendered responses are combined in this way, a zero pressure field should result. This is indeed the case if a single anechoic response is subtracted to counteract the doubling of the continuing sound source within the modelled domain from the sum of $C_R(\theta)$ and $D(\theta)$. The right-most panel of Figure 6 shows the resulting zero-pressure wave field. As demonstrated here, the directional sound source approach has been shown as applicable to negative directivity function weights.

CASE 5: Summing Random Target and Inverse Target Directivity Responses to Produce a Monopole Response

In this final test case, the directional sound source implementation is applied to reproduce a highly directional, complex directivity function. The method is as follows: a target directivity pattern is generated by assigning a random number in the range [0:1] to $S(\theta)$ (denoted $R(\theta)$) for every contributing boundary node. The correctness of the result is then verified by also simulating the directivity given by 1 - $R(\theta)$ (with some abuse of terminology, referred to here as the "inverse" of $R(\theta)$). The sum of the two resulting wave fields after the first reflection should then be equal to that rendered by the monopole $M(\theta)$. The target directivity functions are shown in Figure 7 below and the results of simulation in Figure 8 overleaf.

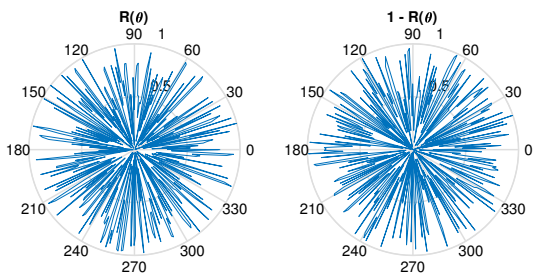

Figure 7: The complex directivity function $R(\theta)$ plotted over the azimuth against degrees alongside its inverse 1-$R(\theta)$.

As shown in Figure 8, the two wave fields rendered in response to the directivity functions $R(\theta)$ and 1-$R(\theta)$ sum together to pro-

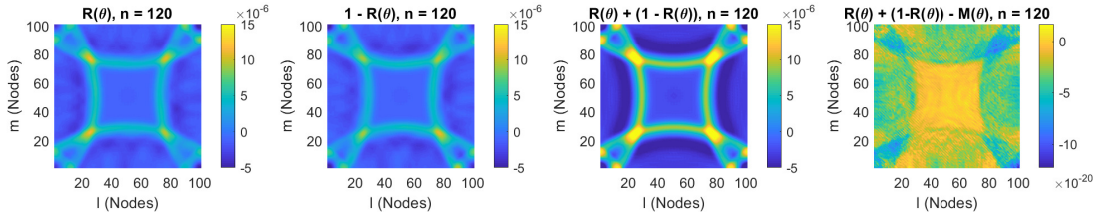

Figure 8: Results of CASE 5. (From left to right) The wave fields rendered in response to directivity functions $R(\theta)$, $1 - R(\theta)$, their sum and the difference between the sum and the monopole $M(\theta)$.

duce a monopole reflection pattern (third panel from the left). As per the previous test cases, the addition of more than one rendered wave field results in an excess of the continuing sound source within the summed pressure field. Hence, in this case a single anechoic response is subtracted from the sum of $R(\theta)$ and $1 - R(\theta)$ prior to rendering the comparison with $M(\theta)$ as shown in the right most panel of Figure 8. Given that a zero pressure field results, it is clear that the sum of the two responses to the complex directional source functions equates that of a monopole. As such, this method has been demonstrated as capable of representing highly complex source directivities.

5. LIMITATIONS OF CURRENT APPROACH

This research has focused primarily on the derivation and proof-of-concept work undertaken to establish the basis for future refinement of the directive source approach. While the approach is shown to deliver encouraging results in a simple concave domain, there are limitations on its usage in acoustic modeling. Firstly, the source strategy is well suited to modeling scenarios in which detailed source directivity functions are sought but the source location and directivity function must remain static for each simulation. Secondly, the approach is limited to application in concave domain geometries for directivities that are consistent across the simulated bandwidth. However, at high frequencies (i.e. those at which diffraction may be neglected) this model may be extended to arbitrary domains through manipulation of transfer functions at boundary nodes that have a direct line of sight to the source location.

6. CONCLUSION

A directional sound source excitation method for IR rendering in FDTD acoustic models has been formulated and shown to provide correct results for a range of test cases and target directivity functions. This approach may be used for static source IR rendering to produce simulations of increased accuracy when complex sound source directivity functions are a primary concern (i.e. room acoustics modeling and virtualization). Future work will focus on improving validation approaches, addressing known limitations and extending the method to 3D acoustics modelling, frequency-dependent source directivity characteristics and multiple simultaneous directional source excitations. Futhermore, the computational overheads of applying the weighting functions during simulation run-time remain to be assessed.

7. ACKNOWLEDGEMENTS

The author wishes to thank the anonymous reviewers for their helpful and detailed input to the preparation of this manuscript and the shaping of future work on this problem.

8. REFERENCES

[1] J. Escolano, J. J. Lopez, and B. Pueo, "Broadband directive sources for acoustic discrete-time simulations," *J. Acoust. Soc. Am.*, vol. 126, no. 6, pp. 2856–2859, December 2009.

[2] J. Escolano, J. J. Lopez, and B. Pueo, "Directive sources in acoustic discrete-time domain simulations based on directivity diagrams," *J. Acoust. Soc. Am.*, vol. 121, pp. EL256–EL262, May 2007.

[3] A. Southern and D. Murphy, "Low complexity directional sound sources for finite difference time domain room acoustic models," in *126th Audio Eng. Soc. Conv.*, May 2009.

[4] F. Georgiou and M. C. J. Hornikx, "Incorporating source directivity in the pseudospectral time-domain method by using spherical harmonics," in *43rd International Congress on Noise Control Engineering*, January 2014.

[5] R. Mehra, L. Antani, and D. Manocha, "Source directivity and spatial audio for interactive wave-based sound propagation," in *20th Int. Conf. on Auditory Display (ICAD)*, June 2014.

[6] H. Hacıhabiboğlu, B. Gunel, and A. M. Kondoz, "Time-domain simulation of directive sources in 3D digital waveguide mesh-based acoustical models," *IEEE Trans. Audio, Speech, Lang. Process.*, vol. 16, no. 5, pp. 934–946, July 2008.

[7] S. Bilbao and B. Hamilton, "Directional source modelling in wave-based room acoustics simulation," in *IEEE Workshop on Applications of Signal Processing to Audio and Acoustics*, October 2017, pp. 121–125.

[8] S. Bilbao and B. Hamilton, "Directional Sources in Wave-Based Acoustics Simulation," *IEEE/ACM Transations on Audio, Speech and Language Processing*, vol. 27, no. 2, pp. 415–428, February 2019.

[9] D. Takeuchi, K. Yatabe, and Y. Oikawa, "Source directivity approximation for finite-difference time-domain simulation by estimating initial value," *J. Acoust. Soc. Am.*, vol. 145, no. 4, pp. 2638–2649, April 2019.

[10] K. Kowalczyk and M. van Walstijn, "Room acoustics simulation using 3-D compact explicit FDTD schemes," *IEEE Trans. Audio, Speech, Lang. Process.*, vol. 19, no. 1, pp. 34–46, April 2011.

[11] K. Kowalczyk and M. van Walstijn, "Formulation of locally reacting surfaces in FDTD/K-DWM modelling of acoustic spaces," *Acta Acustica united with Acustica*, vol. 94, pp. 891–906, September 2008.

[12] H. Kuttruff, *Room Acoustics*, Taylor Francis, London, 5 edition, 2009.

[13] J. Botts and L. Savioja, "Spectral and pseudospectral properties of finite difference models used in audio and room acoustics," *IEEE/ACM Trans. Audio, Speech, Lang. Process.*, vol. 22, no. 9, pp. 1403–1412, June 2014.

[14] C. J. Webb and S. Bilbao, "Computing room acoustics with CUDA - 3D FDTD schemes with boundary losses and viscosity," in *IEEE Int. Conf. on Acoustics, Speech and Signal Process.*, May 2011, pp. 317–320.

[15] J. Escolano, C. Spa, Adán Garriga, and T. Mateos, "Removal of afterglow effects in 2-D discrete-time room acoustics simulations," *Applied Acoustics*, vol. 74, no. 6, pp. 818–822, June 2013.

[16] S. Bilbao and J. O. Smith, "Finite difference schemes and digital waveguide networks for the wave equation: stability, passivity, and numerical dispersion," *IEEE Trans. Audio and Speech Process.*, vol. 11, no. 3, pp. 255–266, May 2003.

[17] K. Kowalczyk, *Boundary and medium modelling using compact finite difference schemes in simulations of room acoustics for audio and architectural design applications*, Ph.D. thesis, Queen's University Belfast, November 2008.

[18] K. Kowalczyk and M. van Walstijn, "Wideband and isotropic room acoustics simulation using 2-D interpolated FDTD schemes," *IEEE Trans. Audio, Speech, Lang. Process.*, vol. 18, no. 1, pp. 78–89, February 2010.

[19] D. Murphy, A. Southern, and L. Savioja, "Source excitation strategies for obtaining impulse responses in finite difference time domain room acoustics simulation," *Appl. Acoustics*, vol. 82, pp. 6–14, August 2014.